nature materials

Article

https://doi.org/10.1038/s41563-023-01670-6

Long-term stability of aerophilic metallic surfaces underwater

Received: 19 December 2022

Accepted: 21 August 2023

Published online: 18 September 2023

Check for updates

Alexander B. Tesler[1] ✉, Stefan Kolle[2,3], Lucia H. Prado[1], Ingo Thievessen[4], David Böhringer[4], Matilda Backholm[5], Bhuvaneshwari Karunakaran[5], Heikki A. Nurmi[5], Mika Latikka[5], Lena Fischer[4], Shane Stafslien[6], Zoran M. Cenev[5], Jaakko V. I. Timonen[5], Mark Bruns[1], Anca Mazare[1,7], Ulrich Lohbauer[8], Sannakaisa Virtanen[1], Ben Fabry[4], Patrik Schmuki[1,9], Robin H. A. Ras[5,10], Joanna Aizenberg[2,3] & Wolfgang H. Goldmann[4] ✉

Aerophilic surfaces immersed underwater trap films of air known as plastrons. Plastrons have typically been considered impractical for underwater engineering applications due to their metastable performance. Here, we describe aerophilic titanium alloy (Ti) surfaces with extended plastron lifetimes that are conserved for months underwater. Long-term stability is achieved by the formation of highly rough hierarchically structured surfaces via electrochemical anodization combined with a low-surface-energy coating produced by a fluorinated surfactant. Aerophilic Ti surfaces drastically reduce blood adhesion and, when submerged in water, prevent adhesion of bacteria and marine organisms such as barnacles and mussels. Overall, we demonstrate a general strategy to achieve the long-term stability of plastrons on aerophilic surfaces for previously unattainable underwater applications.

Wetting describes the ability of liquids to maintain contact with a solid surface, a phenomenon that is ubiquitous in nature[1]. However, in engineering and medical applications, the contact of a solid surface with water can lead to undesirable phenomena such as corrosion, chemofouling and biofouling[2], which have extremely negative economic, health and environmental impacts[3,4]. Therefore, controlling wetting on solid surfaces is key to mitigating its detrimental effects. Although wetting is a macroscopic process, it is sensitive to surface properties at the molecular level. Thus, wetting is also strongly influenced by surface topography. High surface roughness in combination with low-surface-energy materials leads to the formation of non-wettable, so-called super-hydrophobic surfaces (SHS)[5]. SHS, which combine a microscale/nanoscale rough surface topography with low-surface-energy chemistry, can trap air between their protrusions when immersed in water, a situation termed a plastron, and such surfaces are also called aerophilic surfaces (APhS)[6]. SHS have been researched for decades to overcome wetting challenges[7]; however, they are still rarely used in engineering applications mainly due to two drawbacks. First, highly textured rough surfaces are mechanically weaker than their smooth analogues and thus easily abraded[8]. This drawback of SHS has recently been addressed by various strategies[8–11]. Second, a much less resolved drawback is that the non-wetting

[1]Department of Materials Science and Engineering, Institute for Surface Science and Corrosion WW4-LKO, Friedrich-Alexander-Universität Erlangen-Nürnberg, Erlangen, Germany. [2]Wyss Institute for Biologically Inspired Engineering, Harvard University, Cambridge, MA, USA. [3]John A. Paulson School of Engineering and Applied Sciences, Harvard University, Cambridge, MA, USA. [4]Department of Physics, Biophysics Institute, Friedrich-Alexander-Universität Erlangen-Nürnberg, Erlangen, Germany. [5]Department of Applied Physics, School of Science, Aalto University, Espoo, Finland. [6]Department of Coatings and Polymeric Materials, North Dakota State University, Fargo, ND, USA. [7]Advanced Institute for Materials Research (AIMR), National University Corporation Tohoku University (TU), Sendai, Japan. [8]Department of Operative Dentistry and Periodontology, Friedrich-Alexander-Universität Erlangen-Nürnberg, Erlangen, Germany. [9]Regional Centre of Advanced Technologies and Materials, Palacky University, Olomouc, Czech Republic. [10]Department of Bioproducts and Biosystems, School of Chemical Engineering, Aalto University, Espoo, Finland. ✉e-mail: alexander.tesler@fau.de; wolfgang.goldmann@fau.de

https://doi.org/10.1038/s41563-023-01670-6

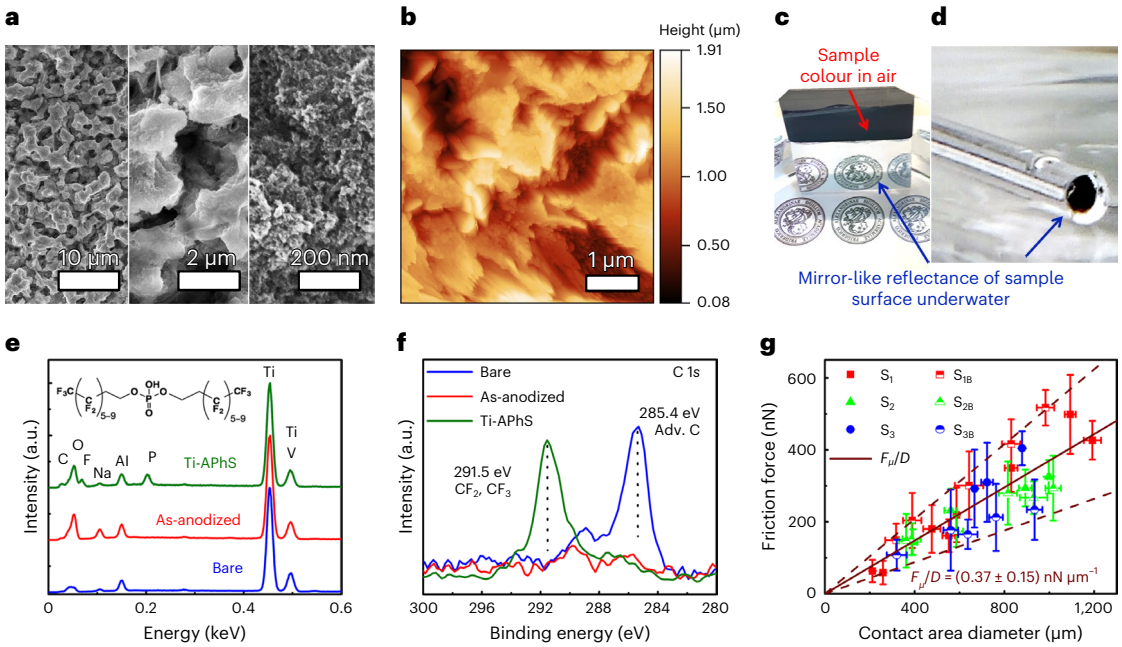

Fig. 1 | Physicochemical characteristics of Ti-APhS. a,**b**, High-resolution top-view SEM images (**a**; increasing magnification from left to right) and AFM images (**b**) of Ti-APhS. **c**,**d**, Digital images of Ti-APhS prepared on sheets (**c**) and rods (**d**) show mirror-like reflectivity underwater. The rod Ti-APhS are 2 mm in diameter. **e**,**f**, EDS spectra (**e**) and high-resolution XPS C 1*s* spectra (**f**) of bare, as-anodized and Ti-APhS samples. **g**, Sliding friction force (F_μ) as a function of drop contact area diameter (D; for water drops of different sizes) on Ti-APhS was probed on both sides of the samples and obtained by the MFS. The abbreviations S_1 and S_{1B} represent the front and back of sample 1 (of 3), respectively. Each data point corresponds to one MFS measurement, where the kinetic friction force has been averaged over a minimum of 1 cm of the sample scanning, corresponding to a minimum of 600 data points. The error for the friction force is the standard deviation (s.d.) of the force data calculated in the same region as the average, and the error for the contact area diameter is the s.d. of the contact area diameter during the scanning experiment. Adv. C, adventitious carbon.

properties degrade over time due to the metastable performance of the plastron, which arises from the coexistence of different energy states[12,13]. Such a metastable performance is even more critical when APhS are submerged in water, since the air trapped between the protrusions disappears over time[14]. As a result, the long-term stability of such surfaces underwater has been considered inadequate for many engineering applications, especially for biofouling prevention[14]. Thus, the long-term stability of a plastron remains the 'Achilles heel' in the implementation of technology involving SHS or APhS[15]. Furthermore, it is even more challenging to produce mechanically robust SHS/APhS with a stable plastron by a facile, inexpensive and scalable process. However, in biology, several species have evolved unique approaches to maintain entrapped air underwater for long periods[16–19].

Here, we report aerophilic surfaces formed on a widely used titanium alloy (Ti-6Al-4V, composed of 90% titanium, 6% aluminium and 4% vanadium) and referred to as Ti-APhS that result in an unprecedented plastron stability exceeding 208 days of continuous submersion underwater. Our Ti-APhS are produced by an industry-standard electrochemical anodization technique followed by modification with a commercially available fluorinated surfactant. We demonstrate that Ti-APhS are extremely blood repellent and drastically reduce or prevent the adhesion of bacteria and marine organisms such as mussels and barnacles. The resulting surface roughness and interfacial energy give rise to a thermodynamically stable aerophilic regime, as predicted by existing theories[20–22]. This work provides experimental evidence and confirmation of the theory, demonstrating that long-term entrapment of air on engineered SHS is feasible for a wide range of applications.

Physicochemical characteristics of Ti-APhS

Ti-APhS were prepared by electrochemical anodization of the Ti-6Al-4V alloy. The anodization cell consists of stainless steel as the counter electrode, Ti alloy as the working electrode and an aqueous solution of $NaOH/H_2O_2$ as the electrolyte. Ti substrates were used as received without any pretreatment other than cleaning (Methods). To obtain a TiO_2 layer of high roughness, two reactions should occur simultaneously: (1) electrochemical oxidation of the metal surface to form an oxide layer, and (2) chemical dissolution of the formed oxide in the same electrochemical environment to increase porosity and create nanoscale roughness (Supplementary Fig. 1 and Supplementary Section 1)[23]. Scanning electron microscopy (SEM), atomic force microscopy (AFM) and transmission electron microscopy (TEM) of Ti-APhS confirm the hierarchical structure of randomly oriented, irregularly shaped micrometre-scale protrusions with a subtle, nanoscale rough surface of anodized TiO_2 (Fig. 1a,b and Supplementary Figs. 2 and 3). The bare and as-anodized Ti substrates are shown in Supplementary Figs. 4 and 5. X-ray diffraction spectroscopy and high-resolution TEM confirm the formation of a rough amorphous TiO_2 layer (Supplementary Fig. 6). The APhS coating can be deposited on both flat and curved Ti substrates such as sheets, foils, rods and coils (Fig. 1c,d).

A water droplet deposited on the as-anodized Ti substrate completely wets it with a water contact angle (WCA) of 0°; that is, it is super-hydrophilic (Supplementary Video 1). Super-hydrophobic (in Cassie–Baxter wetting regime, that is, aerophilic) Ti surfaces (that is, Ti-APhS) were obtained by immersing the as-anodized Ti substrates in a container of 1 wt% commercial phosphate ester fluorinated alkyl chain surfactant (FS) solution under ambient conditions[11]. Polyfluoroalkyl and perfluoroalkyl substances are regulated due to their chemical stability, which leads to bioaccumulation[24]. Therefore, to minimize the waste of fluorinated compounds, the FS solution was used several times for a period of >3.5 years without showing any signs of degradation in its coating performance. Energy-dispersive X-ray spectroscopy (EDS; Fig. 1e and Supplementary Figs. 2 and 3) and X-ray photoelectron spectroscopy (XPS; Fig. 1f, Supplementary Figs. 7 and 8 and Supplementary Table 1) show the typical peaks attributed to bare, as-anodized and

https://doi.org/10.1038/s41563-023-01670-6

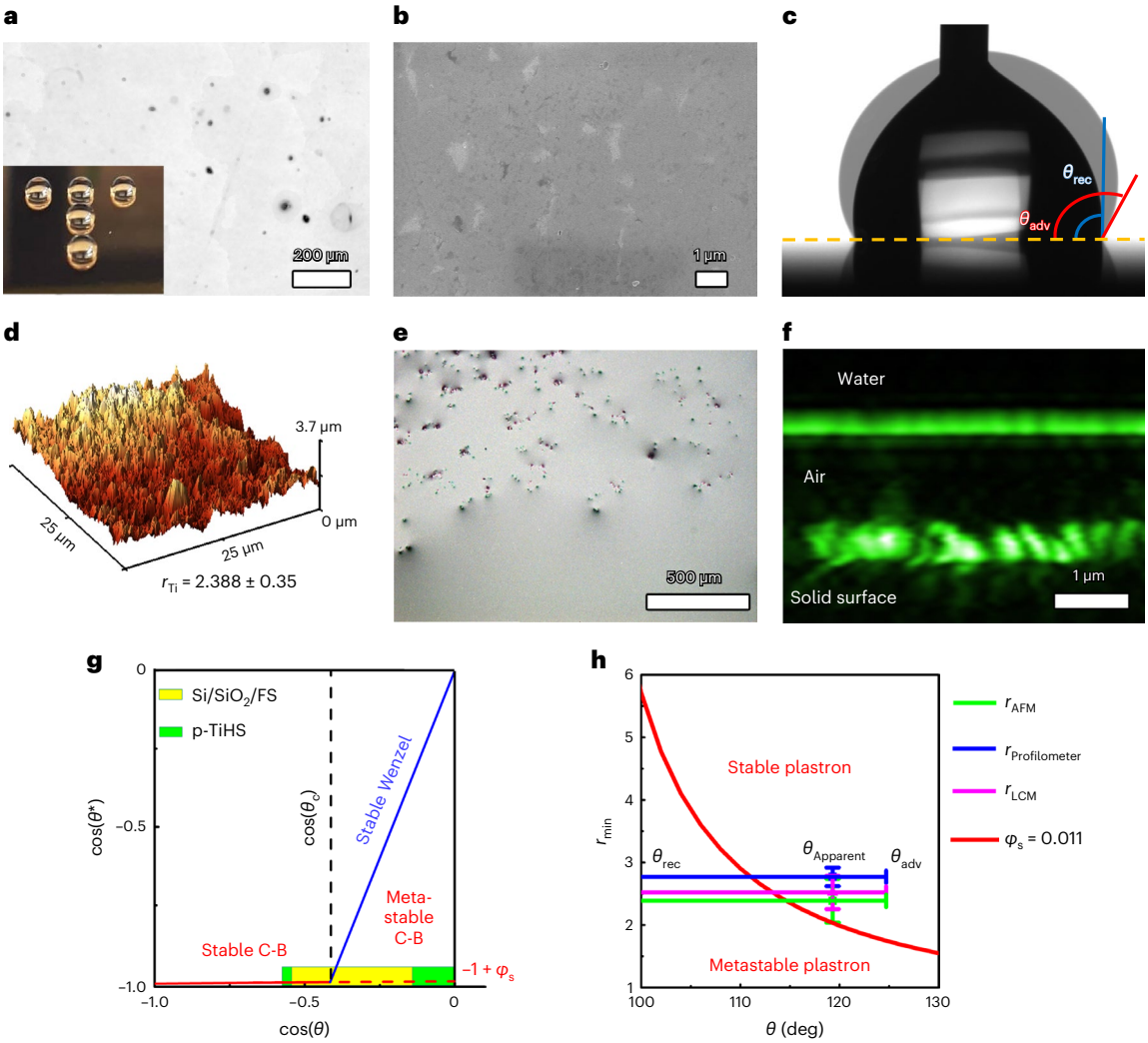

Fig. 2 | Quantifying the wetting regime of Ti-APhS. a–**c**, Top-view laser confocal image (**a**) and SEM image (**b**), and corresponding advancing and receding CAs (**c**) measured on the polished FS-modified Ti alloy (p-TiHS). The image in **c** is a composite of advancing and receding CA measurements. Inset in **a** is a digital image of the polished FS-modified Ti alloy with mirror-like reflectance. **d**, Typical three-dimensional (3D) reconstruction image of the roughness of Ti-APhS (r_{Ti}) obtained by AFM. **e**, A typical bright-field reflectance microscopy image of Ti-APhS underwater. **f**, A confocal cross-sectional image of the plastron on Ti-APhS underwater. **g**, The apparent WCA ($\cos(\theta^*)$) predicted by the Wenzel and Cassie–Baxter (C-B) models as a function of the most stable WCA ($\cos(\theta)$) based on the solid–liquid area fraction as measured on Ti-APhS. The stable Cassie–Baxter wetting regime (red line) changes at the critical CA ($\cos(\theta_c)$) to a stable Wenzel regime (blue line) or metastable Cassie–Baxter regime (red dashed line). The shaded green area represents the possible wetting regimes of Ti-APhS measured on p-TiHS and compared to the FS-modified Si/SiO_2 wetting system (Si/SiO_2/FS, yellow area). **h**, Minimum roughness (r_{min}), measured by AFM (r_{AFM}), optical profilometer ($r_{Profilometer}$) and laser confocal microscopy (r_{LCM}) on Ti-APhS, required for a stable underwater plastron for a maximum $\varphi_s = 0.011$ (corresponding to the upper limit of the liquid–solid area fraction) as a function of the most stable WCA (θ). The most stable advancing and receding CAs and roughness parameter were measured on $N = 3$ independent samples, while the data represent the measured average value and the s.d.

Ti-APhS samples, confirming the binding of the fluorinated surfactant to the anodized TiO_2. Interestingly, the as-anodized Ti samples do not show an adventitious carbon peak even after months of ageing in ambient atmosphere (Fig. 2f), as is commonly observed on TiO_2 nanostructures due to the adsorption of contaminating molecules from air[25].

The wetting properties of Ti-APhS were investigated. Ti-APhS exhibit mirror-like uniform reflectance underwater due to the air plastron (Fig. 1c,d), in contrast to their as-anodized counterparts, which are non-reflective (Supplementary Fig. 9). They are ultra-slippery, with an apparent WCA of 170.0° ± 8.6° and a sliding angle of 0.7° ± 0.3°. The data were obtained using a conventional goniometer. However, the measurements were not reliable simply because water droplets tend to roll off Ti-APhS quickly (Supplementary Video 2). It has also been shown that for ultra-slippery surfaces, a substantial change in the measured WCA values occurs when the fitting baseline is shifted by even a single pixel[26]. Here, alternative approaches were used to confirm and estimate the ultra-slipperiness of Ti-APhS with greater accuracy. A micropipette force sensor (MFS), which measures the frictional force of water droplets on ultra-slippery SHS (Fig. 1g, Supplementary Fig. 10a and Supplementary Video 3)[27], and an oscillating droplet tribometer (ODT), which measures the frictional force between the SHS and the test droplet over a centimetre range[28], confirm the ultra-slipperiness of Ti-APhS. We also compared Ti-APhS to state-of-the-art SHS, and the dimensionless friction force measurements placed Ti-APhS among the most slippery of the engineered SHS studied, demonstrating uniformity over the entire sample area (Supplementary Fig. 10b).

Typically, non-wettable surfaces are described by an apparent contact angle (CA) and CA hysteresis. However, this approach is not accurate enough to describe ultra-slippery surfaces and especially their plastron stability underwater. Therefore, another methodology

https://doi.org/10.1038/s41563-023-01670-6

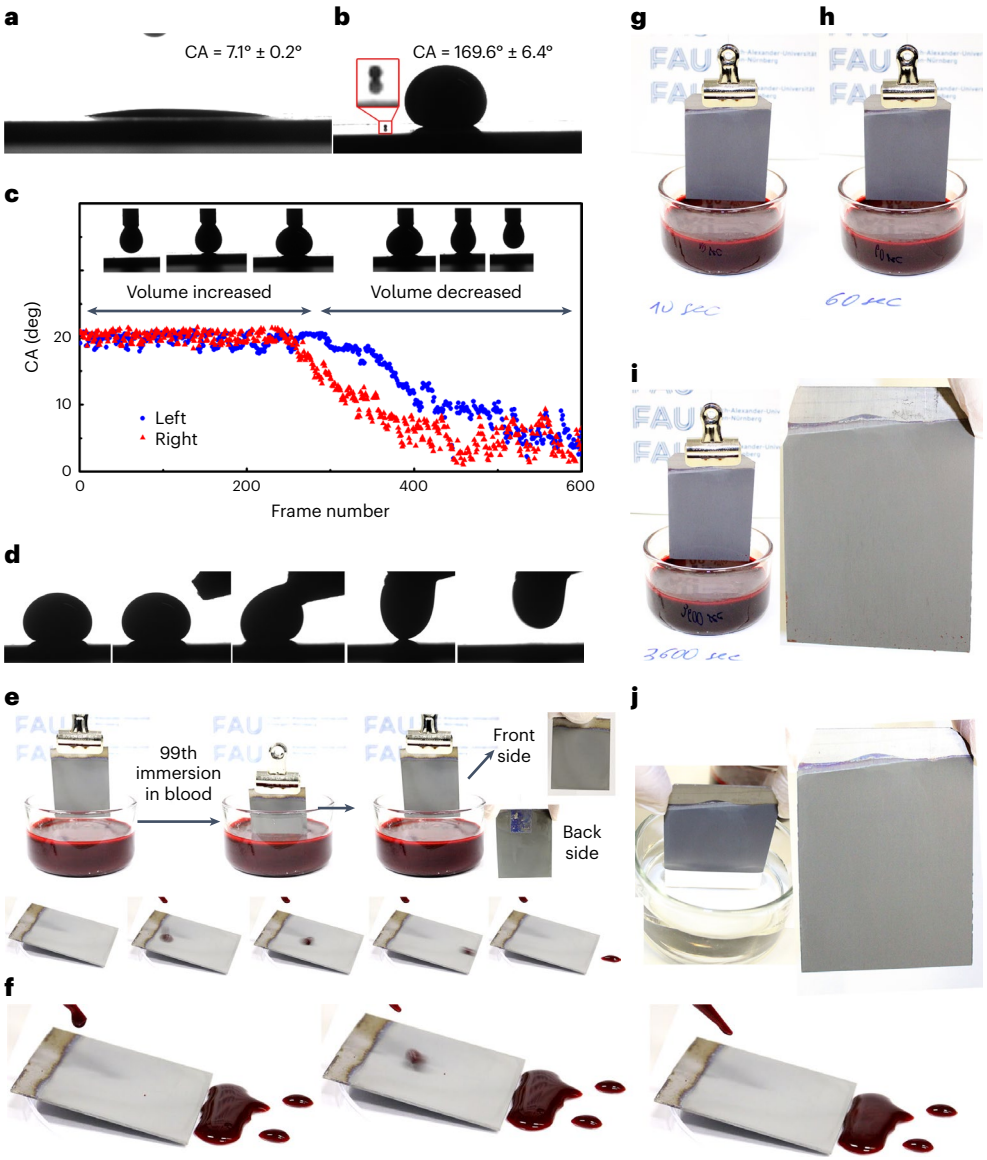

Fig. 3 | Blood repellency of Ti-APhS. a,**b**, CA of fresh blood on as-anodized sample (**a**) and Ti-APhS (**b**). **c**, Advancing and receding CA measurements on Ti-APhS. Inset images show droplet shape with increasing and decreasing blood droplet volume. **d**, Snapshot digital images of the blood droplet wiped off Ti-APhS with a tissue. **e**, Digital images of Ti-APhS before, during and after 99 times of immersion in fresh blood. **f**, Blood dropped on the Ti-APhS shown in **e**. **g**,**h**, Ti-APhS after immersion in fresh blood for 10 s (**g**) and 60 s (**h**). **i**,**j**, Still digital images of the sample immersed in fresh blood for 3,600 s (**i**) followed by a brief rinse in water (**j**).

should be applied to accurately characterize the wetting regime of such materials. This has been proposed by Lafuma and Quéré for SHS[21], and theoretically calculated by Marmur for underwater aerophilicity[20,22]. In both approaches, each non-wettable surface should be described by (1) the Young's CA, estimated by measuring the most stable CA on a smooth substrate of the same hydrophobic origin, (2) the surface roughness (the ratio of actual to projected surface area) and (3) the solid–liquid area fraction (the actual contact area between water and the solid surface, that is, the pinning points). To be useful for real engineering applications, such SHS/APhS should also be mechanically robust[13].

Ti-APhS were studied by both approaches to characterize their wetting regime. First, we estimated the most stable WCA (θ) on FS-modified Ti alloy substrates polished to a mirror-like state (p-TiHS). Note that it is impossible to polish metallic samples to atomic resolution. The roughness of p-TiHS was evaluated by laser confocal microscopy and found to be 1.005 ± 0.001 (Fig. 2a,b). The most stable WCA is the apparent CA related to the lowest Gibbs energy for a given system[29], where the CAs are believed to approach Young's values. However, there is no common method to accurately measure the most stable CA, while a measurable CA could be any value between the advancing and receding CAs, which are the highest and lowest metastable apparent CAs. Here, the most stable WCA of the p-TiHS lies between the advancing (θ_{adv} = 124.4° ± 0.8°) and receding (θ_{rec} = 82.9° ± 4.0°) CAs (Fig. 2c and Supplementary Fig. 11.1). For example, when a water droplet was deposited on p-TiHS, the apparent WCA was 119.3° ± 2.6°. By comparison, the advancing and receding WCAs on the FS-modified 100-nm-thick SiO_2 on a Si wafer with nanoscale roughness were 122.6° ± 1.4° and 97.0° ± 3.6°, respectively (Supplementary Fig. 11.1g–i).

The surface roughness (r) of Ti-APhS was obtained by laser confocal microscopy and further confirmed by AFM and an optical confocal white-light sensor profilometer (Fig. 2d and Supplementary Fig. 11.2). While all techniques confirm a similar roughness within standard deviation measurements, the lowest value of 2.388 ± 0.35 was obtained by AFM. Finally, we measured the solid–liquid area fraction

https://doi.org/10.1038/s41563-023-01670-6

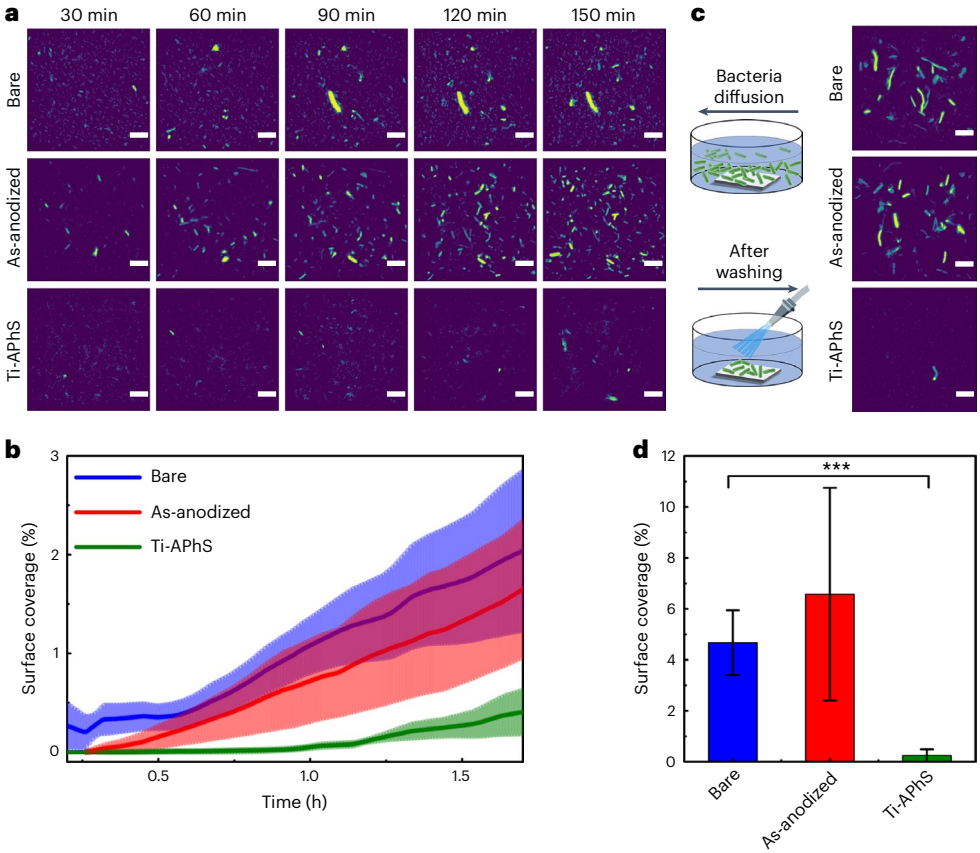

Fig. 4 | Bacterial repellence of Ti-APhS. a, Time-lapse images of non-motile live GFP-expressing *E. coli* on bare, as-anodized and Ti-APhS samples. Scale bars, 10 µm. **b**, Surface coverage on the samples shown in **a**. Line width (shading) indicates mean ± s.d. measured from three independent biological replicates. **c**,**d**, Images (**c**, right) and surface coverage (**d**) of non-motile bacteria on the samples shown in **a** after 4 h of bacterial exposure and subsequent washing (depicted in the schematics on the left in **c**; ***$P < 0.001$ ($P = 1.4 \times 10^{-9}$) obtained by the Welch's *t*-test). The statistical analysis was obtained from $N = 3$ independent samples, while five fields of view per sample were stored and analysed. Scale bars, 10 µm.

(φ_s) using bright-field reflectance microscopy, while the Ti-APhS were immersed underwater. The solid–liquid area fraction was found to be 0.0054 ± 0.0047, indicating that the plastron covers ~99% of the surface (Fig. 2e and Supplementary Fig. 11.3). Cross-sectional confocal microscopy images confirmed the presence of the plastron (Fig. 2f).

The wetting of liquids on rough solid surfaces is described in terms of the balance of the interfacial Gibbs energies of the solid, liquid and vapour phases. Two wetting regimes, that is, Wenzel (homogeneous or fully wetted, also known as the pinning regime) and Cassie–Baxter (heterogeneous or composite surface of vapour and solid, that is, aerophilic, also known as the slippery regime), can coexist on the same substrate (Fig. 2g, blue and dashed red lines), while the relative value of the Gibbs energy minima and the barrier between them depends on the chemical nature of the surface, the particular surface topography and the wetting liquid[13,22]. It is generally accepted that plastrons on artificial SHS are metastable. This means that a transition from the Cassie–Baxter to the Wenzel wetting regime often occurs, especially underwater[12]. To adequately evaluate the wetting regime as well as the stability of the plastron underwater, we applied the methods proposed by Lafuma and Quéré[21] and Marmur[20,22]. In the first case, the critical (threshold) CA (θ_c) between the two wetting regimes was calculated from $\cos(\theta_c) = (\varphi_s - 1)/(r - \varphi_s)$ and was found to be $\theta_c = 114.5° \pm 4.5°$ (Fig. 2g)[21]. Any value of Young's WCA higher than θ_c indicates the formation of the stable Cassie–Baxter wetting regime, while SHS with values lower than θ_c may exhibit either stable Wenzel or metastable Cassie–Baxter wetting. Based on the calculations and considering the limitations of the most stable CA measurements, it is suggested that Ti-APhS may exhibit a stable Cassie–Baxter wetting regime (Fig. 2g, shaded green rectangular area). To validate the underwater stability of the plastron, calculations proposed by Marmur were applied, where thermodynamic equilibrium and stability conditions were formulated to minimize the solid–liquid contact area[20]. It was postulated that for a sufficiently high roughness ratio (r_{min}), the plastron is feasible and thermodynamically stable. The results are shown in Fig. 2h for the upper limit of the measured φ_s for Ti-APhS, that is, 1.1% of the solid–liquid area fraction. This methodology also shows that the obtained roughness of Ti-APhS, as well as the hydrophobic nature of the surfactant, can raise Ti-APhS above the minimum roughness condition required for a stable plastron underwater (further discussion is in Supplementary Section 11).

The aerophilic lifetime of Ti-APhS was evaluated as follows: (1) Ti-APhS trapped air bubbles for more than 208 days of continuous submersion; this experiment is still ongoing as of this writing, with no signs of degradation (Supplementary Fig. 11.4 and Supplementary Video 4). (2) When submerged at a 50 cm depth, Ti-APhS exhibited an aerophilic Cassie–Baxter regime for 14 days, while after 67 days, ~10% of the area had changed to the Wenzel regime (Supplementary Fig. 11.5 and Supplementary Video 5). The latter is 36 times longer than any state-of-the-art APhS submerged at 50 cm depth (assuming at least 50% plastron failure; Supplementary Table 2). A plastron lifetime of 30 days has previously been reported as ultra-stable[30], while periods longer than 50 days have been defined as an infinite plastron lifetime[31]. (3) Ti-APhS floated on water for 133 days due to the plastron, while without a plastron, the sample sank immediately (Supplementary Fig. 11.6).

https://doi.org/10.1038/s41563-023-01670-6

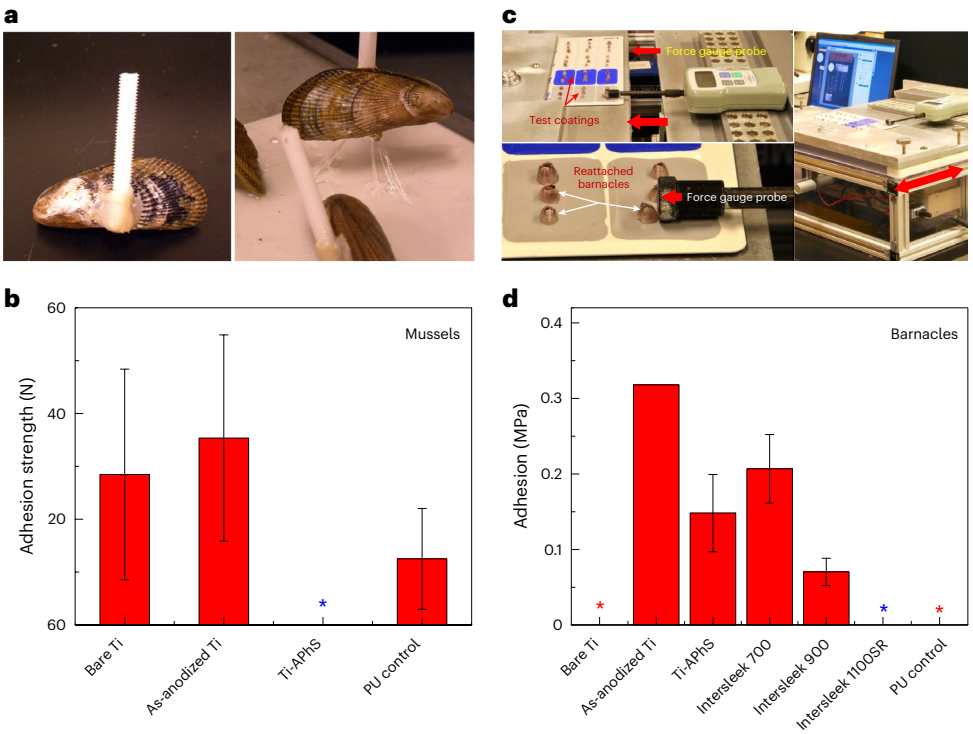

Fig. 5 | Marine anti-biofouling characteristics of Ti-APhS. a, Mussel (*G. demissa*) adhesion test to determine the forces required to remove the mussel from the substrate. **b**, Mean mussel adhesion strength on bare, as-anodized (super-hydrophilic), Ti-APhS and polyurethane (PU) control samples. The blue star indicates that the mussels failed to adhere to the coating surface. Error bars show s.d.; $N = 6$. **c**, Adult barnacle (*A. amphitrite*) reattachment test set-up. **d**, Mean adult barnacle adhesion to bare, as-anodized (super-hydrophilic), Ti-APhS and polyurethane control samples, as well as samples with commercial anti-biofouling coatings (Intersleek 700, 900 and 1100SR). The blue star indicates that the barnacles did not reattach to the coating surface; the red stars indicate that the barnacle shell and/or base plate broke during the test and remained on the coating surface, that is, a coating failure. Error bars show s.d.; $N = 6$.

These results demonstrate that APhS with sufficient roughness can effectively trap and retain an air plastron underwater for months.

The excellent water repellency of Ti-APhS is mainly due to the stable plastron. Yet, mechanical robustness is essential for their use in engineering applications, especially underwater. The mechanical durability of Ti-APhS has been studied by water jet impact (70 psi), bending, linear abrasion[9] and sand[32] abrasion, mimicking harsh outdoor conditions. Ti-APhS retain their wetting properties under hot-water and cold-water jets (the calculated water jet force was 8.98 N, equivalent to ~900 g of mass impacting the surface; Supplementary Video 6), bending, twisting (Supplementary Video 7) and sand abrasion by hard and heavy particles (Supplementary Fig. 12 and Supplementary Video 8). Ti-APhS retain a CA greater than 150° after 20 cycles of linear abrasion by a stainless steel block, although the sliding angle increases (Supplementary Fig. 13). The combination of a chemically bonded (intrinsic) TiO_2 with irregularly shaped amorphous protrusions minimizes damage propagation over a large area, allowing Ti-APhS to exhibit excellent resistance to compressive and tensile stresses[11].

Blood repellency of Ti-APhS

Blood is a highly challenging fluid to repel due to its tendency to activate intrinsic haemostatic mechanisms, induction of coagulation and platelet activation upon contact with a foreign body[33]. Imbalanced activation of coagulation influences the formation of blood clots (thrombogenesis), which can obstruct blood flow and expose tissues to ischaemia and infarction. Blood-repellent SHS aim to reduce the thrombogenicity of blood-contacting devices and implants by minimizing their contact with blood. The main challenge is the long-term stability of the slippery wetting regime under physiological conditions as the plastron tends to disappear.

Since the Ti alloy used in this study is the most widely used material for implants, we investigated the blood-repellent properties of Ti-APhS by immersing them in a container of blood (Fig. 3). As shown in Fig. 3a–c, the Ti-APhS have an apparent blood CA of 169.6° ± 6.4° and a CA hysteresis of ~14°, indicating very low blood adhesion (Supplementary Video 9). Sessile blood droplets on Ti-APhS can be easily removed with a paper wipe, leaving a clean surface free of blood traces (Fig. 3d and Supplementary Video 10). We performed a sequential immersion of Ti-APhS in blood 99 times, keeping them immersed for 1 s during each cycle (Fig. 3e). The bare Ti surface (control) was completely covered by blood after the first immersion (Supplementary Fig. 14a,b and Supplementary Video 11). Here, the Ti-APhS are evenly coated on both sides and edges due to the preparation process. Potentiostatic current transients confirmed the continuity of the plastron (details are in Supplementary Section 15, Supplementary Fig. 15 and Supplementary Video 12). Ti-APhS immersed 99 times were completely free of blood on both sides and edges (Fig. 3e and Supplementary Fig. 14c,d). Figure 3f shows blood droplets rolling off on the Ti-APhS sample after 99 immersions, confirming the stability of the plastron (Supplementary Video 13). By comparison, FS-modified aluminium SHS, which had similar wetting characteristics but a different morphology and mechanical robustness, lost the plastron after only a few seconds of exposure to blood (Supplementary Video 14).

The blood-repellent longevity of Ti-APhS was assessed by the subsequent immersion in a container of blood for different lengths of time (Fig. 3g–i). Ti-APhS were completely free of blood after 0.8 h of immersion, while several small blood spots were observed after 1.8 h and removed by a brief rinse in water (Fig. 3j and Supplementary Fig. 14e–g). The unique blood repellency of Ti-APhS is attributed to

the synergy between plastron stability (enabled by surface topography and chemistry) and mechanical robustness.

Bacterial repellency of Ti-APhS

Due to the increase in human life expectancy, metallic implants made of Ti-6Al-4V have become common practice in orthopaedic and dental surgery[34]. However, the implant surfaces are prone to bacterial fouling and biofilm formation, which are difficult to remove even with antibiotics, potentially leading to severe postoperative surgical site infections[35]. Biofilms grow on a solid surface covered by fluid[36]; therefore, reducing the contact between a solid surface and a fluid containing bacteria, such as APhS, is expected to affect biofilm formation and growth. We investigated bacterial adhesion by exposing Ti-APhS to green fluorescent protein (GFP)-expressing *Escherichia coli* (*E. coli*), while using bare, as-anodized (super-hydrophilic) and bare-FS-modified (hydrophobic) substrates as controls. It has been shown that *E. coli* flagellar filaments facilitate adhesion to wetted rough surfaces, allowing them to penetrate crevices and form a dense, fibrous network within a short period of time[14,37]. Live confocal microscopy revealed a steady increase in bacterial coverage on all control surfaces but coverage to a much lesser extent on Ti-APhS (Fig. 4a,b, Supplementary Fig. 16 and Supplementary Video 15). Sliding time window analysis was applied to identify non-motile bacteria as opposed to floating bacteria captured on a single image. This revealed a consistent increase in surface coverage of the controls, while Ti-APhS showed little bacterial accumulation (Fig. 4a). Quantification of bacterial surface coverage confirmed a similar increase on all control substrates, while Ti-APhS showed only a small increase (Fig. 4b).

To investigate whether the non-motile *E. coli* represent bacteria adhering to the surface rather than bacteria trapped in the developing biofilm, all of the examined surfaces were washed and analysed using a short sliding time window (Fig. 4c). As shown, bacteria covered a large portion of the control samples even after washing, confirming that our assay detected adherent bacteria. By contrast, the few bacteria covering Ti-APhS after the exposure period were almost completely removed after washing (Fig. 4d). This demonstrates the inability of bacteria to infiltrate and adhere to Ti-APhS due to the stable air plastron caused by a very small liquid–solid area fraction. Furthermore, these data confirm that (1) prolonged immersion of rough surfaces underwater promotes bacterial adhesion during long-term exposure, (2) the fluorinated surfactant is generally non-toxic to bacteria and allows comparable biofilm formation as demonstrated on bare Ti surfaces and (3) Ti-APhS with their stable plastron retard bacterial biofilm formation of *E. coli*.

Marine anti-biofouling performance of Ti-APhS

Preventing marine organism adhesion is considered a particularly challenging application for non-adhesive surfaces due to the short life of the plastron (Supplementary Table 2)[14]. Here, we assess the protective nature of the stable plastron of Ti-APhS underwater when exposed to some of the most challenging marine organisms, such as mussels and barnacles, known as hard foulers. This is because marine mussels are able to adhere firmly to wet organic and inorganic surfaces through the secretion of mussel foot proteins[38], while barnacles secrete a multi-protein complex called biocement that hardens at the adhesion site and is insoluble in water[39]. The marine biofouling set-ups and results are summarized in Fig. 5. As shown, mussel (*Geukensia demissa*) adhesion was completely prevented by Ti-APhS over the three-day experimental immersion period (Fig. 5a,b). Adult barnacle (*Amphibalanus amphitrite*) re-adhesion occurred on Ti-APhS; however, the adhesion strength of the barnacles was remarkably lower on Ti-APhS than on untreated controls and comparable to the fouling release treatment Intersleek 700, that is, a commercial anti-biofouling paint, over the 14-day experimental immersion period (Fig. 5c,d). These results demonstrate that Ti-APhS prevent biofouling over a prolonged period of immersion due to the long-lasting stable plastron, even in the presence of macro-fouling organisms that use proteinaceous adhesives (mussels) and biocement (barnacles). These results further suggest that FS surfactant is non-toxic to marine organisms, as evidenced by a similar amount of barnacle reattachment compared to non-toxic commercial paints.

In conclusion, despite intensive studies of super-hydrophobic (aerophilic) surfaces in the past, the focus of research needs to be adjusted to develop long-lasting stable aerophilic surfaces underwater. While the mechanical robustness of SHS has recently been demonstrated, the metastability of the plastron has not been sufficiently addressed. The transition from a heterogeneous wetting (Cassie–Baxter) regime to a fully wetted (Wenzel) regime within a relatively short period is primarily responsible for the failure of SHS/APhS in general and in particular underwater, promoting undesirable processes such as corrosion, chemofouling and biofouling due to their large surface areas. Here, WCA and CA hysteresis, two main reported quantities, do not provide direct information on plastron stability, making it difficult to predict the aerophilic performance of surfaces underwater. Therefore, characteristics such as surface roughness, solid–liquid area fraction and the most stable CA measured on a smooth surface of the same hydrophobic origin are crucial parameters to shed light on whether the developed APhS are in a stable or metastable slippery wetting regime. Despite decades of research, the study of aerophilic surfaces still requires advanced characterization methods to obtain and ensure an unambiguous interpretation of all the aforementioned parameters. As we show, by determining the plastron stability information, it is possible to extend the performance of APhS underwater for months, inhibiting the attachment of blood, bacteria and marine organisms. Our Ti-APhS demonstrate a similar marine biofouling retention compared to state-of-the-art commercial anti-biofouling paints. The simple and scalable fabrication of uniformly rough Ti-6Al-4V alloy surfaces of various geometries using inexpensive materials and industrial electrochemical techniques, together with a facile approach to surface energy reduction and mechanical robustness, makes this method feasible for biomedical applications. Finally, our approach to creating highly rough Ti surfaces with well-defined uniform morphology can serve as an excellent scientific model for investigating plastron stability to maintain aerophilicity over months to years for highly demanding applications.

Online content

Any methods, additional references, Nature Portfolio reporting summaries, source data, extended data, supplementary information, acknowledgements, peer review information; details of author contributions and competing interests; and statements of data and code availability are available at https://doi.org/10.1038/s41563-023-01670-6.

References

1. Quéré, D. Wetting and roughness. *Annu. Rev. Mater. Res.* **38**, 71–99 (2008).
2. Field, R. in *Membrane Technology* (eds Peinemann, K.-V. & Nunes, S. P.) 1–23 (Wiley-VCH, 2010).
3. Cámara, M. et al. Economic significance of biofilms: a multidisciplinary and cross-sectoral challenge. *npj Biofilms Microbiomes* **8**, 42 (2022).
4. Davis, J. R. in *Corrosion: Understanding the Basics* (ed. Davis, J. R.) Ch. 1, 1–17 (ASM International, 2000).
5. Marmur, A. in *Non-wettable Surfaces: Theory, Preparation and Applications* (eds Ras, R. H. A. & Marmur, A.) 1–11 (The Royal Society of Chemistry, 2017).
6. Rapoport, L., Emmerich, T. & Varanasi, K. K. Capturing bubbles and preventing foam using aerophilic surfaces. *Adv. Mater. Interfaces* **7**, 1901599 (2020).
7. Cassie, A. B. D. & Baxter, S. Wettability of porous surfaces. *Trans. Faraday Soc.* **40**, 546–551 (1944).

8. Lu, Y. et al. Robust self-cleaning surfaces that function when exposed to either air or oil. *Science* **347**, 1132–1135 (2015).
9. Wang, D. et al. Design of robust superhydrophobic surfaces. *Nature* **582**, 55–59 (2020).
10. Peng, C., Chen, Z. & Tiwari, M. K. All-organic superhydrophobic coatings with mechanochemical robustness and liquid impalement resistance. *Nat. Mater.* **17**, 355–360 (2018).
11. Tesler, A. B. et al. Extremely durable biofouling-resistant metallic surfaces based on electrodeposited nanoporous tungstite films on steel. *Nat. Commun.* **6**, 8649 (2015).
12. Poetes, R., Holtzmann, K., Franze, K. & Steiner, U. Metastable underwater superhydrophobicity. *Phys. Rev. Lett.* **105**, 166104 (2010).
13. Chen, F. et al. Robust and durable liquid-repellent surfaces. *Chem. Soc. Rev.* **51**, 8476–8583 (2022).
14. Hwang, G. B. et al. The anti-biofouling properties of superhydrophobic surfaces are short-lived. *ACS Nano* **12**, 6050–6058 (2018).
15. Mehanna, Y. A. et al. The challenges, achievements and applications of submersible superhydrophobic materials. *Chem. Soc. Rev.* **50**, 6569–6612 (2021).
16. Seymour, R. S. & Matthews, P. G. D. Physical gills in diving insects and spiders: theory and experiment. *J. Exp. Biol.* **216**, 164–170 (2013).
17. Srinivasan, S. et al. Quantification of feather structure, wettability and resistance to liquid penetration. *J. R. Soc. Interface* **11**, 20140287 (2014).
18. Yu, C., Zhang, P., Wang, J. & Jiang, L. Superwettability of gas bubbles and its application: from bioinspiration to advanced materials. *Adv. Mater.* **29**, 1703053 (2017).
19. Flynn, M. R. & Bush, J. W. M. Underwater breathing: the mechanics of plastron respiration. *J. Fluid Mech.* **608**, 275–296 (2008).
20. Marmur, A. Underwater superhydrophobicity: theoretical feasibility. *Langmuir* **22**, 1400–1402 (2006).
21. Lafuma, A. & Quéré, D. Superhydrophobic states. *Nat. Mater.* **2**, 457–460 (2003).
22. Marmur, A. & Kojevnikova, S. Super-hydrophobic surfaces: methodological considerations for physical design. *J. Colloid Interface Sci.* **568**, 148–154 (2020).
23. Beranek, R., Hildebrand, H. & Schmuki, P. Self-organized porous titanium oxide prepared in H_2SO_4/HF electrolytes. *Electrochem. Solid State Lett.* **6**, B12 (2003).
24. Cousins, I. T., Johansson, J. H., Salter, M. E., Sha, B. & Scheringer, M. Outside the safe operating space of a new planetary boundary for per- and polyfluoroalkyl substances (PFAS). *Environ. Sci. Technol.* **56**, 11172–11179 (2022).
25. Filippin, N. et al. Plasma-enabled amorphous TiO_2 nanotubes as hydrophobic support for molecular sensing by SERS. *ACS Appl. Mater. Interfaces* **12**, 50721–50733 (2020).
26. Liu, K., Vuckovac, M., Latikka, M., Huhtamäki, T. & Ras, R. H. A. Improving surface-wetting characterization. *Science* **363**, 1147–1148 (2019).
27. Backholm, M. et al. Water droplet friction and rolling dynamics on superhydrophobic surfaces. *Commun. Mater.* **1**, 64 (2020).
28. Timonen, J. V. I., Latikka, M., Ikkala, O. & Ras, R. H. A. Free-decay and resonant methods for investigating the fundamental limit of superhydrophobicity. *Nat. Commun.* **4**, 2398 (2013).
29. Marmur, A., Della Volpe, C., Siboni, S., Amirfazli, A. & Drelich, J. W. Contact angles and wettability: towards common and accurate terminology. *Surf. Innov.* **5**, 3–8 (2017).
30. Thamaraiselvan, C., Manderfeld, E., Kleinberg, M. N., Rosenhahn, A. & Arnusch, C. J. Superhydrophobic candle soot as a low fouling stable coating on water treatment membrane feed spacers. *ACS Appl. Bio Mater.* **4**, 4191–4200 (2021).
31. Xu, M., Sun, G. & Kim, C.-J. Infinite lifetime of underwater superhydrophobic states. *Phys. Rev. Lett.* **113**, 136103 (2014).
32. Deng, X., Mammen, L., Butt, H.-J. & Vollmer, D. Candle soot as a template for a transparent robust superamphiphobic coating. *Science* **335**, 67–70 (2012).
33. Jokinen, V., Kankuri, E., Hoshian, S., Franssila, S. & Ras, R. H. A. Superhydrophobic blood-repellent surfaces. *Adv. Mater.* **30**, 1705104 (2018).
34. Froes, F. H. in *Titanium in Medical and Dental Applications* (eds Froes, F. H. & Qian, M.) 3–21 (Woodhead Publishing, 2018).
35. Chae, K. et al. Antibacterial infection and immune-evasive coating for orthopedic implants. *Sci. Adv.* **6**, eabb0025 (2020).
36. Hall-Stoodley, L., Costerton, J. W. & Stoodley, P. Bacterial biofilms: from the natural environment to infectious diseases. *Nat. Rev. Microbiol.* **2**, 95–108 (2004).
37. Friedlander, R. S. et al. Bacterial flagella explore microscale hummocks and hollows to increase adhesion. *Proc. Natl Acad. Sci. USA* **110**, 5624–5629 (2013).
38. Lee, H., Scherer, N. F. & Messersmith, P. B. Single-molecule mechanics of mussel adhesion. *Proc. Natl Acad. Sci. USA* **103**, 12999–13003 (2006).
39. Kamino, K. Mini-review: barnacle adhesives and adhesion. *Biofouling* **29**, 735–749 (2013).

Methods

Titanium electrochemical anodization

Ti alloy sheets were cut to the following sizes: 25 × 25, 40 × 50, 50 × 60, 50 × 75, 100 × 100, 10 × 200 and 100 × 200 mm. Before anodization, the substrates were cleaned ultrasonically in acetone and ethanol for 10 min to remove contamination. The electrochemical cell consists of a stainless steel (either 304 or 316 grade) counter electrode of similar size to the Ti alloy sheet, a Ti alloy sheet/rod/coil used as a working electrode and a 1.5 M NaOH aqueous solution used as the electrolyte. Then 1 vol% H_2O_2 was added to the NaOH electrolyte just before anodization. The counter and working electrodes were placed 10–20 mm away from each other depending on the sample size. Anodization was carried out at an applied potential of 15 V for 30 min. When using large samples, the cell was kept in a big reservoir of water at room temperature. The anodization process could be repeated up to three times with the same electrolyte. As-anodized samples were then removed from the electrolyte, rinsed with deionized water and dried under a stream of N_2.

Low-surface-energy coating

The fluorinated surfactant FS-100 (10 g) was dissolved in 1 l of 95:5 vol% ethanol/H_2O by ultrasonication and then kept in a closed container under ambient conditions. As-anodized samples were immersed in the FS solution. A plastic cover to prevent ethanol evaporation was used to seal the surfactant container. A container with the samples was placed in a muffle furnace preheated to +60 °C for 30 min. The low-surface-energy Ti substrates (Ti-APhS) were then removed from the FS solution, rinsed with ethanol and dried under a stream of N_2. To obtain the most stable CA, one that is most close to Young's CA, Ti samples were ground with SiC grinding paper (up to 1,200) and then polished with an up to 1 µm diamond suspension. After polishing, the samples were cleaned in an ultrasonication bath with acetone and ethanol. Subsequently, the polished Ti samples were anodized for 5 s at an applied potential of 15 V in NaOH/H_2O_2 electrolyte to form a thin dense TiO_2 layer followed by the standard FS modification procedure.

Characterization techniques

Wetting characterizations. WCA measurements. The apparent WCA measurements, when possible, for Ti-APhS were carried out using an Attension Theta CA goniometer (Biolin Scientific). A small drop was deposited on the surface, its volume was increased to ~10 µl and the WCA was measured. An error of ±5° was added to the obtained s.d. values to include the measurement inaccuracies based on a model, where the droplet baseline is deviated by ±1 pixel level[26]. For roll-off measurements, the drop volume was 10 µl. The tilting speed was 10° per minute, and the image recording was performed at 2.3 frames per second (f.p.s.). All values specified in the text were averaged from at least three independent measurements.

Most stable CA measurements. The most stable WCA measurements were performed using polished (mirror-like) Ti alloy surfaces, anodized for a short time in the regular electrolyte to form a thin dense TiO_2 layer followed by the FS modification (p-TiHS). Since there is no common methodology to determine the most stable CA, we measured advancing and receding CAs, which are the maximum and minimum apparent CA values, respectively. An apparent CA could then be any value between these two limiting values[13]. The advancing and receding WCAs were measured using the DSA100 CA goniometer (KRÜSS) as follows: a drop of 20 µl volume was infused on p-TiHS at a rate of 0.05 µl s^{-1}, the drop of 40 µl was withdrawn on p-TiHS at a rate of 0.05 µl s^{-1} and image recording was performed. The shape of a sessile drop was calculated using the Ellipse method (Tangent-1) by KRÜSS Drop Shape Analysis software. All values specified in the text were averaged from at least three independent measurements. Since it is not possible to polish a metallic surface to atomically smooth topography, we compared the advancing and receding WCA values obtained from p-TiHS with the FS-modified Si/SiO_2 substrates (MicroChemicals GmbH, Si(100) p-type + 100 nm SiO_2) with nanometre-scale roughness.

CA and hysteresis measurements of Ti-APhS immersed long term underwater. The apparent WCA measurements of Ti-APhS immersed at 50 cm depth underwater were carried out using a DSA100 CA goniometer (KRÜSS). Drop Shape Analysis software provided by KRÜSS was applied to fit the droplet profile. The WCA was calculated using the Laplace–Young method of sessile drop. The drop volume was ~10 µl. An error of ±5° was added to the obtained s.d. values to include the measurement inaccuracies based on a model[26]. For CA hysteresis, the drop volume of 10 µl was increased and decreased at a rate of 0.05 µl s^{-1}, and a video was taken. The fitting was performed using the Ellipse method (Tangent-1) using the KRÜSS Drop Shape Analysis software. The calculated values obtained by the Ellipse fitting algorithm for CA hysteresis are lower than those calculated by the Laplace–Young fitting algorithm for the apparent CA; therefore, the difference in the apparent and receding CAs should be considered only as CA hysteresis (not the absolute calculated value). All values specified in the text were averaged from at least three independent measurements.

Confocal microscopy imaging of plastron. Confocal imaging of the plastron was done as described previously with small changes[27]. Briefly, Ti-APhS were imaged using a ×20, 1.0 W (Zeiss) objective lens with a deionized water droplet between Ti-APhS and an objective lens. *Z*-stacks were collected at 200 nm steps while recording reflection images (458 nm laser line) from the sample using a regular upright confocal microscope (Zeiss Examiner LSM710). The confocal pinhole was closed to ~0.1 Airy units to maximize the resolution.

Morphology and physicochemical characterization. For morphological characterization, a field-emission SEM instrument (Hitachi FE-SEM S4800) was used equipped with EDS (EDAX Genesis). X-ray diffraction analysis (X'pert Philips MPD with a Panalytical X'celerator detector) using graphite monochromized Cu Kα radiation (wavelength, 1.54056 Å) was applied for determining the crystallographic composition of the samples. The composition and the chemical state of the films were characterized using XPS (PHI 5600), the spectra were shifted according to the C 1*s* signal at 284.8 eV and peaks were fitted by Multipak software.

Surface roughness measurements. Atomic force microscopy. An AFM NanoWizard from JPK with µMasch HQ:NSC18/Al BS cantilevers was used to obtain the roughness parameters of the samples of Ti-APhS. All images were taken in a.c. mode at a high resolution of 1,024 pixel × 1,024 pixel and a slow line scan rate of ~0.05 Hz. The images were analysed using the Gwyddion software as suggested by the manufacturer. Statistical analysis of the roughness of Ti-APhS was determined from at least three spots and three independent samples.

Optical profilometer. To obtain surface roughness, a high-resolution non-contact white-light profilometer CyberScan CT 100 equipped with a P-CHR-600 sensor that provides a height resolution of 20 nm (Cyber Technologies) was used.

Laser confocal microscopy. A laser confocal microscope (VK-X3100, Keyence) equipped with a laser of λ = 404 nm wavelength was applied. The laser confocal microscope provides a resolution of 0.1 nm in height and width, and an accuracy of <2% from measured values. An optical aperture of ×150 was used to measure spots of 1,000 × 1,000 µm. In all cases, at least four independent spots were measured to obtain statistically relevant values of the roughness.

Solid–liquid area fraction measurements. A polystyrene Petri dish was filled with deionized water to a height of ~1 cm. The samples of Ti-APhS were then immersed underwater and forced to sink to the bottom. The solid–liquid area fraction was obtained using a Nikon Eclipse LV150 microscope equipped with a Nikon DS-Fi1 camera in bright-field reflectance mode.

Mechanical robustness. Linear abrasion test. A TABER Linear Abraser (Abrader) Model 5750 was used with a steel block (AISI 316) as the abradant. The steel block was in contact with the surface of Ti-APhS (contact area of 1.5 × 10 mm) and moved linearly, producing an abraded area of 13 × 10 mm. The force applied was 2.4 N, resulting in a pressure of 0.16 MPa. The speed at the centre of the abraded region was 27 mm s^{-1}. The steel block was moved for 20 cycles to obtain the final abraded region.

Sand abrasion test. Yttria-stabilized zirconia particles (total mass of 35 g, >16,000 particles) with a diameter of 0.8 mm (2.1 mg) impinged the surface from a height of 0.4 m, corresponding to an impinging energy density of 7.8×10^{-6} J, which is two orders of magnitude higher than sand silica particles, and at a velocity of 2.8 m s^{-1} per particle.

Water jetting. Hot or cold water was injected through a 3.9 mm nozzle faucet at 70 psi pressure, equivalent to a water jet velocity of 31.07 m s^{-1}. The impinging force was calculated as follows: $F = \rho \times A \times U^2$, where ρ is the water density, A is the nozzle area and U is the jet velocity. The calculated impinging force was 8.98 N, which is equivalent to ~900 g of impinging mass.

Bending and twisting of Ti-APhS. Ti-APhS prepared on foil with an area of of 10 × 200 mm and thickness of 250 µm were soldered to hard handles at both ends, which enabled us to bend and twist it underwater to identify plastron stability (the reflectivity of the surface due to the plastron) under compressive and tensile stresses.

Micropipette force sensor measurements. The contact-line friction of water drops moving on the samples of Ti with SHS/APhS was probed using MFS according to a previously developed protocol[27]. In short, straight micropipette cantilevers were manufactured from thick glass capillaries (inner diameter/outer diameter, 0.75 mm:1 mm; World Precision Instruments) using a micropipette puller (Narishige) and cutting it with a microforge (Narishige). The cantilevers were calibrated using a water droplet of different volumes as a control weight[40]. The MFS used in this work had a spring constant of $k_p = 12.0 \pm 0.2$ nN µm^{-1}, where p means pipette. In friction experiments, the sample to be probed was placed on a motorized xyz stage, and the MFS cantilever was vertically mounted above the sample. The entire set-up was mounted on an active anti-vibration table (Halcyonics_i4large, Accurion) to damp the noise. A Canon 90D camera with a Canon MP-E macro lens was mounted at the side to image the drop and micropipette at 60 f.p.s. At first, a MilliQ water drop was placed on the glass micropipette also to rest on the surface. The sample was shifted in the y direction (away from the camera) to place the micropipette in its equilibrium ($F = 0$ nN) position. The camera was then triggered (to first capture the $F = 0$ nN position of the MFS) and ~4 s later, the motor started moving at velocity $v = 0.1$ mm s^{-1} in the x direction (to the side, as viewed from the camera). The sample was scanned for ~20 s before the camera was turned off and the motor stopped. Analysing the deflection (Δx) of the force-calibrated micropipette, the force was calculated as $F = k_p \Delta x$. The contact-line friction (F_μ) was determined by taking an average of the force data in the sliding friction regime (Supplementary Fig. 10a). MFS friction experiments were performed on both sides of three different samples using different drop volumes ($V = 1$–10 µl). The friction force was compared to the contact area diameter (D), which was measured with side-view videos. The resulting F_μ versus D graph is shown in Fig. 1g of the main manuscript, where the linear F_μ/D slope represents the slipperiness of the sample, that is, a lower slope indicates higher slipperiness. As shown in Supplementary Fig. 10b, $F_\mu/\gamma D$ (γ, surface tension) is plotted for different samples to show how Ti-APhS compared to other SHS.

Oscillating droplet tribometer measurements. ODT measurements on samples of Ti-APhS were performed using a previously described protocol[41]. The ODT measures the friction and the viscous forces affecting a water-like ferrofluid droplet from the oscillation motion of the droplet. The ferrofluid droplet oscillates in a harmonic magnetic potential well at zero vertical component formed with two permanent magnets. The oscillation of the droplet is caused by moving the permanent magnets in a sinusoidal fashion for two oscillations near the resonance frequency of the ferrofluid droplet. The motion of the droplet was captured using a Phantom V1610 high-speed camera at 1,000 f.p.s., and the droplet location was determined as the droplet centroid using Matlab script. The droplet centroid motion was then fitted to an analytical model of the general harmonic oscillator by viscous and friction force[28]. The viscous coefficient and friction force were obtained from the fit. The Ti-APhS were characterized using 5 µl ferrofluid droplets with an iron oxide nanoparticle concentration of 0.2 vol%. Three different Ti-APhS were measured ten times on the same spot. The ODT measures a slightly larger dimensionless friction ($F_\mu/\gamma D$) compared to MFS (Supplementary Fig. 10b). This is due to the ODT measurement scanning a region of centimetre scale, averaging over all different pinning sites at varying friction force values.

Blood adhesion experiments. Fresh pig's blood was provided by Unifleisch. Sodium citrate (0.5 vol%) was added to the fresh blood to prevent clotting. The tubes were then placed on a circular rotator at 20 r.p.m. for 5 min to homogenize the content prior to experimentation. Ti-APhS were sequentially immersed 99 times (RDC 15 Dip Coater, Bungard Elektronik) in the container containing blood and holding it for 1 s every cycle. For time dependent measurements, the Ti-APhS were sequentially immersed in the container containing blood for 1, 5, 10, 30, 60, 300, 600, 1,800 and 3,600 s. After 3,600 s in blood, the sample was immersed in the container with water. Blood CA measurements were performed by a CA measurement system (DSA100, KRÜSS) at room temperature. The droplet volume for the measurements was 5–10 µl, and the macroscopic droplet profile was captured on camera. The droplet profile was fitted by Drop Shape Analysis software provided by KRÜSS. The apparent blood CA was calculated using the Laplace–Young method for a sessile droplet. Note that the blood droplet shape is asymmetrical; therefore, an error of ±5° was added to the obtained s.d. values to include the measurement inaccuracies based on the Laplace–Young fitting model. All CA values specified in the text were averaged from at least three independent measurements. The CA hysteresis of the blood droplet was analysed using a custom CA analysis algorithm, which has been validated against commercial software for super-hydrophobic surfaces[27,40,41]. The code analyses the CAs with the polynomial tangent method, which is one of the commonly used methods among Laplace–Young and circular fit[42–44]. In the analysis, a frame of the video is initially cropped so that only the droplet and its reflection are visible. This cropped image is turned black and white by thresholding the illumination value such that the droplet and its reflection are white, and the background is black. This allows one to search for the edge of the droplet as the points where the pixels change from black to white or white to black. The baseline is found as the thinnest part between the droplet and its shadow. A fourth-degree polynomial is fitted to the edge points of the droplet on each side separately, and the CA is calculated as the tangent of the polynomial at the baseline level. The baseline is assumed horizontal to the video, which causes errors in the measurement if the sample is tilted.

Anti-bacterial characterizations. Bacterial stock preparation. *E. coli* (DH-5alpha) expressing cytoplasmic GFP were generated using the pGLO bacterial transformation kit (Bio-Rad). The stock culture was generated from an agar stock plate, from which one or two colonies were transferred to growth medium. All cultures were incubated overnight at 37 °C in 5 ml Tryptic Soy Broth growth medium (Becton Dickinson) and kept shaking continuously in an orbital shaker at a speed of 150 turns min^{-1}. The concentration of bacteria was measured by UV–visible spectroscopy at a wavelength of 600 nm (optical density, OD_{600nm}) versus pure medium (control) and calculated

according to the following equation: 1.000 OD_{600nm} = 8×10^8 CFU ml^{-1} (CFU, colony-forming unit; ref. 45).

Confocal microscopy analysis of bacterial attachment. Bare (untreated) samples, as-anodized samples and Ti-APhS (25 × 25 mm) were imaged using an upright laser scanning confocal microscope system (Leica, SP5) using a ×20, 1.0 numerical aperture, dip-in objective lens. Material samples for all surfaces were mounted in a 10 cm cell culture dish and immersed in 30 ml LB medium (Carl Roth). Five fields of view per material sample were stored for time-lapse imaging before substitution of 15 ml LB medium by 15 ml GFP-expressing *E. coli* bacteria suspension in 0.5% L-arabinose at an optical density of ~1.000. Subsequently, fluorescent image stacks (74 × 74 µm and 6–20 µm depth) were recorded at each position over 3.5–4.5 h (frame rate, 3–7 min). Image stacks were maximum projected prior to analysis using Python-based image processing[46]. Non-motile bacteria were distinguished from diffusive bacteria using a sliding time window analysis. Non-motile bacteria were determined for each time window by calculating the lower quartile of the pixel intensity distribution across the time steps included in the respective time window (23–30 min, corresponding to 3–7 consecutive frames), resulting in images in which pixels are bright only when the original signal is high over time, that is, non-motile bacteria. Yen thresholding across the last images of every surface was used to segment non-motile bacteria with one common threshold for each experiment[47]. After time-lapse imaging, the bacteria suspension was removed and samples were washed three times with phosphate-buffered saline, followed by short time-lapse imaging for three consecutive frames, which were maximum projected and analysed again by single time window analysis of the lower quartile pixel intensity distribution as described above. Welch's *t*-test, which assumes unequal variances, was applied to calculate statistical significance.

Marine anti-biofouling characterizations. Barnacle reattachment and adhesion. The bare samples, as-anodized (super-hydrophilic) samples, Ti-APhS, polyurethane control (polyurethane standard prepared at North Dakota State University[48]) and commercially available anti-biofouling paints Intersleek 700, 900 and 1100SR were used to assess the reattachment and adhesion of barnacles. Five adult barnacles (*A. amphitrite*) of testable size (>5 mm basal diameter) were dislodged from glass panels coated with Silastic T2 and placed on coated 100 × 200 mm Ti-APhS and control plates. Immobilization templates were then applied to each panel to anchor barnacles to the coated surfaces and then transferred to an artificial saltwater aquarium tank system. The reattached barnacles were fed daily with freshly hatched brine shrimp nauplii (*Artemia* sp.). After 14 days of reattachment in the aquarium system, the samples were removed from an artificial seawater aquarium tank and mounted on a semi-automated push-off device to measure the peak adhesion force of the reattached barnacles during release from the surface. The area of the barnacle base plates was measured using SigmaScan Pro software package (SigmaScan Pro 5.0, Systat Software). The adhesion strength was calculated by normalizing the detachment shear force to the basal area. Barnacle adhesion for each coating was reported as the mean value of the total number of barnacles that had a measurable detachment force. Barnacles that had no measurable force for detachment were counted as 'not attached' and not included in adhesion calculations.

Marine mussel attachment and adhesion. Freshly collected adults of the ribbed mussel *G. demissa* (3–5 cm in size) were obtained from Duke University Marine Laboratory in Beaufort, North Carolina, USA, and housed in an Aquarium Society of Winnipeg (ASW) aquarium tank system with continuous monitoring and maintenance of pH (8.0–8.2) and salinity (35 ppt). Prior to attachment studies, a 4 cm section of acetal plastic rod (product no. 98873A105, McMaster-Carr) was adhered to the shell of each mussel, perpendicular to the ventral edge, using a 3M acrylic adhesive (product no. 7467A135, McMaster-Carr). Custom-designed templates fabricated from polyvinyl chloride sheets were then used to immobilize six mussels each onto the coated 100 × 200 mm Ti-APhS and control plates, using set-screws to firmly secure the adhered, plastic rods. The samples were placed in the ASW aquarium system, and the mussels were fed daily with live marine phytoplankton (DTs Premium Reef Blend Phytoplankton). After three days of immersion, the mussels were removed from the ASW aquarium tank system, and the total number of mussels exhibiting attachment of byssus threads was recorded for each surface. The rod of each attached mussel was then secured to an individual 5 N load cell of a custom-built, tensile force gauge outfitted with six loads of cells to enable simultaneous measurements of all attached mussels. The total force required to detach the byssus threads for each mussel was recorded (1 mm s^{-1} pull rate) and the average pull-off force value (in newtons) for all attached mussels was calculated for each coating surface.

Data availability

All data are available in the main text or Supplementary Information. All relevant data are available from the corresponding authors upon reasonable request.

References

40. Backholm, M. & Bäumchen, O. Micropipette force sensors for in vivo force measurements on single cells and multicellular microorganisms. *Nat. Protoc.* **14**, 594–615 (2019).
41. Junaid, M., Nurmi, H. A., Latikka, M., Vuckovac, M. & Ras, R. H. A. Oscillating droplet tribometer for sensitive and reliable wetting characterization of superhydrophobic surfaces. *Droplet* **1**, 38–47 (2022).
42. Akbari, R. & Antonini, C. Contact angle measurements: from existing methods to an open-source tool. *Adv. Colloid Interface Sci.* **294**, 102470 (2021).
43. Huhtamäki, T., Tian, X., Korhonen, J. T. & Ras, R. H. A. Surface-wetting characterization using contact-angle measurements. *Nat. Protoc.* **13**, 1521–1538 (2018).
44. Orella, M. J., Leonard, M. E., Román-Leshkov, Y. & Brushett, F. R. High-throughput analysis of contact angle goniometry data using DropPy. *SoftwareX* **14**, 100665 (2021).
45. Myers, J. A., Curtis, B. S. & Curtis, W. R. Improving accuracy of cell and chromophore concentration measurements using optical density. *BMC Biophys.* **6**, 4 (2013).
46. Rausch, M. et al. Measurement of skeletal muscle fiber contractility with high-speed traction microscopy. *Biophys. J.* **118**, 657–666 (2020).
47. Jui-Cheng, Y., Fu-Juay, C. & Shyang, C. A new criterion for automatic multilevel thresholding. *IEEE Trans. Image Process.* **4**, 370–378 (1995).
48. Benda, J. et al. Studying the effect of pre-polymer composition and incorporation of surface-modifying amphiphilic additives on the fouling-release performance of amphiphilic siloxane-polyurethane coatings. *ACS Appl. Mater. Interfaces* **14**, 37229–37247 (2022).

Acknowledgements

We thank A. Marmur for fruitful discussions on the plastron stability of Ti-APhS. A.B.T. thanks N. Vogel and J. Harrer for help with AFM measurements and E. Alkhateeb for help with X-ray diffraction measurements. A.B.T. thanks F. Krause from Keyence Deutschland GmbH for providing a laser confocal microscope for surface roughness measurements. W.H.G. and A.B.T. are indebted to L. Nicholson (Master of Arts) for proofreading the manuscript. We acknowledge the provision of facilities and technical support by Aalto University at OtaNano's Nanomicroscopy Center (Aalto-NMC). A.B.T., P.S., W.H.G. and B.F. thank the Deutsche Forschungsgemeinschaft (DFG; SCHM 1597/38-1 and FA 336/13-1) for their financial support. A.B.T. acknowledges the Emerging Talents Initiative (ETI) of the

Friedrich-Alexander-Universität Erlangen-Nürnberg (grant agreement number 5500102). This work was funded in part by grants from the German Science Foundation (DFG; FA 336-12/1, TRR-SFB 225 Projects A01 and C02). J.V.I.T. acknowledges funding from the Academy of Finland Center of Excellence Program (2022–2029) in Life-Inspired Hybrid Materials (LIBER), project number 346112. M. Backholm acknowledges postdoctoral funding from the Academy of Finland (grant agreement number 309237). M. Bruns, B.K., H.A.N., M.L., Z.M.C., J.V.I.T. and R.H.A.R. acknowledge funding from the Academy of Finland Center of Excellence Program (2022–2029) in Life-Inspired Hybrid Materials (LIBER, project number 346109). S.S. acknowledges funding from the Office of Naval Research, US Department of Defense (grant N00014-17-1-2153). S.K. and J.A. acknowledge funding from the Office of Naval Research, US Department of Defense (grants N00014-15-1-2323 and N00014-17-1-2913) and the Department of Energy (award DE-SC0005247).

Author contributions

A.B.T. conceived the original idea for the project. A.B.T. developed the anodization method to form highly rough aerophilic Ti substrates with hierarchical structures and analysed the formation mechanisms. A.B.T. and S.K. screened and down-selected different coating compositions and fabrication methods, discovering the most promising designs for further study. A.M. performed XPS characterizations. A.B.T., L.H.P. and M. Bruns performed the plastron longevity characterization. A.B.T., L.H.P., M. Backholm, B.K., H.A.N. and M.L. performed the wetting characterization and analysed the experimental data. A.B.T., I.T., L.F., D.B., B.F. and W.H.G. performed the anti-blood adhesion and anti-bacterial characterizations. A.B.T., Z.M.C. and J.V.I.T. performed the SEM, TEM and confocal microscopy characterizations. U.L. carried out the optical profilometry characterization. S.K. and S.S. performed the marine anti-biofouling characterization. A.B.T., S.K., B.F., S.V. and W.H.G. wrote the manuscript. A.B.T., S.K., R.H.A.R., B.F., P.S., S.V., J.A. and W.H.G. discussed the results and revised the manuscript. All authors contributed to the manuscript.

Competing interests

The authors declare no competing interests.

Additional information

Supplementary information The online version contains supplementary material available at https://doi.org/10.1038/s41563-023-01670-6.

Correspondence and requests for materials should be addressed to Alexander B. Tesler or Wolfgang H. Goldmann.

Peer review information *Nature Materials* thanks Björn Wickman and the other, anonymous, reviewer(s) for their contribution to the peer review of this work.